Turbulent structure at the midsection of an annular flow

S. Ghaemi[1], S. Rafati[1], M. Bizhani[2], and E. Kuru[2]

[1] *Department of Mechanical Engineering, University of Alberta, Edmonton, T6G 2G8, Canada*

[2] *School of Mining and Petroleum Engineering, University of Alberta, Edmonton, T6G 2W2, Canada*

The turbulent flow in the midsection of an annular gap between two concentric tubes at Reynolds number of 59,200 to 90,800 based on hydraulic diameter (d_h = 57 mm) and average velocity is experimentally investigated. Measurements are carried out using particle tracking velocimetry (PTV) and planar particle image velocimetry (PIV) with spatial resolution of $0.0068d_h$ (size of the binning window) and $0.0129d_h$ (size of the interrogation window), respectively. Both PTV and PIV results show that the location of maximum mean streamwise velocity (y_U) does not coincide with the locations of zero shear stress (y_{uv}), minimum streamwise velocity fluctuation (y_{u2}) and minimum radial velocity fluctuation (y_{v2}). The separation between y_U and y_{uv} is $0.013d_h$ based on PTV while PIV underestimates the separation distance as $0.0063d_h$. Conditional averages of turbulent fluctuations based on the four quadrants across the annulus demonstrate that the inner and outer wall flows overlap in the midsection. In the midsection, the flow is subject to opposing sweep/ejection events originating from both the inner and outer walls. The opposite quadrant events of the two boundary layers cancel out at y_{uv} while the local minimum of spatial correlation of u (maximum mixing of the two wall flows) occurs at y_U. Investigation of the budget of Reynolds shear stress showed that production and advection terms acts towards the coincidence of the y_U and y_{uv} while the dissipation term works against the coincidence of the two points. The location of $<U>_{max}$ also overlaps with zero dissipation of $<uv>$. The production of turbulent kinetic energy is slightly negative in the narrow region between y_U and y_{uv}. This negative production acts towards smoothing the mean velocity profile at the joint of the two wall flows by equalizing its curvature ($\partial^2<U>/\partial y^2$) on the two sides of y_U. The small separation distance of the y_U and y_{uv} is associated with slight deviation from the fully developed condition.

I. INTRODUCTION

The flow in the annular gap between two concentric tubes is of engineering and fundamental interest. The removal of cutting material in the annular passage between the drill shaft and the well casing is dominated by the mechanisms of the turbulent flow [1]. The convective heat transfer in a double-pipe heat exchanger is another widespread application of annular flow [2]. The fundamental importance of

this flow configuration is mostly associated with its asymmetric velocity profile formed by the interaction of two turbulent wall flows with different spatial and temporal scales.

The asymmetry in the velocity profile of an annular flow was first observed by Brighton & Jones [3] who found that the maximum average velocity ($<U>_{max}$) is not at the midpoint of the annular gap (r_m). In an annular flow, $<U>_{max}$ is at y_U between the inner wall (r_1) and mid-location (r_m) as shown in Figure 1. The asymmetry is also observed in the profile of Reynolds shear stress ($\tau_{uv} = -\rho <uv>$) as $\tau_{uv} = 0$ is located at y_{uv} between r_1 and r_m. However, it is still not clear whether y_U and y_{uv} overlap [4]. This non-coincidence is of fundamental interest since a narrow region of negative turbulence production forms between y_U and y_{uv} [5]. In contrast to a symmetric pipe or channel flow in which y_U and y_{uv} are found to overlap.

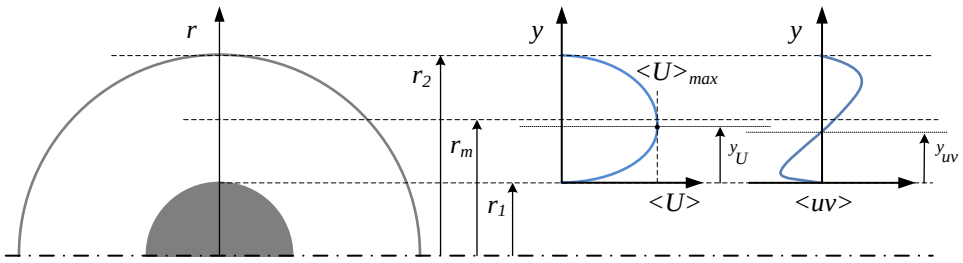

FIG 1. Schematic of the cross-section of a concentric annulus and profiles of average velocity $<U>$ and Reynolds shear stress $<uv>$. The non-coincidence of y_U and y_{uv} in asymmetric profiles is still under debate.

Brighton & Jones [3] carried out measurement of y_U and y_{uv} in annuli with different hydraulic diameters, $d_h = 2\ (r_2\text{-}r_1)$. The location of y_U was obtained from measurement of velocity gradient using two adjacent Pitot tubes which were $0.027d_h$ till $0.57d_h$ apart and y_{uv} from hot-wire measurement. They reported that the deviation of the location of y_U and y_{uv} is within the measurement uncertainty. Lawn & Elliott [6] also used the same measurement combination and observed maximum $y_U - y_{uv}$ of approximately $0.01d_h$ for $Re = 3\times10^4$ and 3×10^5, respectively. Reynolds number is defined based on average velocity (U_b) and hydraulic diameter (d_h) for this experiment and the following works on turbulent annular flow. The deviation of $y_U - y_{uv}$ was observed to increase as the asymmetry of the profile increases with reduction of r_1/r_2. No significant variation of $y_U - y_{uv}$ was observed with change of Reynolds number at a fixed r_1/r_2. Rehme [7] carried out an experimental investigation to measure the location of y_U and y_{uv}

using a double Pitot tube and hot-wire anemometry. It was also observed that y_U and y_{uv} do not coincide at Re = 2×10^4 to 2×10^5 for r_1/r_2 = 0.02 to 0.1. Nouri *et al.* [1] applied laser-Doppler velocimetry and observed that $y_U - y_{uv}$ at Re of 8,900 and 26,600 is within the measurement precision. The recent experiment of Rodriguez-Corredor *et al.* [8] also shows non-coincidence of the two points using PIV measurement for Re range of 17,700 to 66,900. The consensus of the experimental investigations is towards non-coincidence of y_U and y_{uv}. However, the spatial resolution of the applied measurement techniques, intrusion of the spacers holding the inner tube and vibration of the inner tube are among the possible uncertainty sources.

Numerical simulations of the turbulent annuli flow have also shown contradictory results regarding y_U and y_{uv} locations. The direct numerical simulation (DNS) of Chung *et al.* [9] was conducted at a similar condition as the experiment of Nouri *et al.* [1], both at Re = 8,900. This DNS showed non-coincidence of y_U and y_{uv}. However, Boersma & Breugem [4] recently observed the coincidence of the two positions based on a DNS of fully developed turbulent annuli flow with r_1/r_2 of 0.1 at Re = 8,900 to 13,940. Boersma & Breugem [4] associated the non-coincidence observed by Chung *et al.* [9] to poor radial resolution.

The possible non-coincidence of y_U and y_{uv} is also observed in asymmetric turbulent channel flows formed by roughening of one of the walls. Hanjalić & Launder [10] scrutinized the location of y_U and y_{uv} across Re number (based on channel width) of 1.8×10^4 to 8×10^4 using hot-wire anemometry. Their results showed $(y_U - y_{uv}) / W$ to be approximately 10% and almost constant for the investigated channel widths and Re numbers. Nagano *et al.* [11] reported smaller $(y_U - y_{uv}) / W$ of 2.0, 2.8, and 0.8% at three Reynolds numbers between Re = 10^3 - 10^4. Burattini *et al.* [12] carried out a combined experimental and numerical investigation at Re = 3,600, 7,100, and 13,000 and reported indistinguishable y_U and y_{uv} locations. The evidence provided by the previous experimental and numerical investigations on the relative location of y_U and y_{uv} in turbulent annuli flow and in general in asymmetric turbulent profiles still appears inconclusive. It is interesting to also mention that all the investigations which reported non-coincidence of

the two points, y_{uv} is more inclined towards the thinner boundary layer in comparison to y_U ($y_{uv} < y_U$ in annuli flow or y_{uv} closer to the smooth wall in asymmetric channel flows). This trend suggests a possible systematic mechanism causing the lack of overlap instead of measurement/numerical uncertainties.

Turbulence production is typically positive across one-dimensional shear flows, i.e., positive $\partial\langle U\rangle/\partial y$ occurs where $\langle uv\rangle$ is negative. This combination results in a positive gain of turbulence from the mean flow since $-\langle uv\rangle\partial\langle U\rangle/\partial y$ is positive [13]. In an asymmetric profile, if y_U and y_{uv} do not coincide, both $\partial\langle U\rangle/\partial y$ and $\langle uv\rangle$ would have a similar sign in the region of $y_{uv} < y < y_U$ (see Figure 1). This results in a localized zone of negative turbulence production which has also been observed in a number of flow fields with asymmetric mean velocity profile including flow in curved channel [14], wall jet [15, 16], asymmetric channel flow with rough wall on one side [5, 10], asymmetric turbulent wake [17], and separating flows [18]. This region has also been referred to as a zone of energy reversal by Eskinazi and Erian [19] since the negative production term suggests transfer of energy from turbulent fluctuations to the mean flow. This zone precludes both the eddy viscosity model and the Prandtl's mixing length theory. The eddy viscosity (ϵ) is defined in analogy with molecular transport in gases [20] according to

$$-\rho\langle uv\rangle = \epsilon\frac{\partial\langle U\rangle}{\partial y}. \tag{1}$$

In this equation, positive $\langle uv\rangle$ and positive $\partial\langle U\rangle/\partial y$ would result in a negative ϵ which lacks any physical meaning. The Prandtl's mixing length (l) also cannot be estimated in this region following

$$-\rho\langle uv\rangle = \rho l^2\frac{\partial U_m}{\partial y}\left|\frac{\partial U_m}{\partial y}\right|. \tag{2}$$

Although the success of these models in accurate modeling of turbulent flows has been limited to simple flows, the fundamental concept used to develop these models is frequently visited in classical fluid mechanics.

To the authors' knowledge, the only physical explanation for the non-coincidence is provided by Rehme [21] who proposed turbulence diffusion as the cause of the non-coincidence. It was conjectured that diffusion of turbulence plays a stronger role in an asymmetric turbulent channel flow relative to the symmetric profiles in pipes and parallel plates. Chung *et al.* [9] studied the effect of wall curvature on the near-wall turbulent structure and the budget of Reynolds stress in a turbulent annular flow using DNS. They observed smaller turbulent intensities and Reynolds stresses on the inner wall compared to those of the outer wall. Burattnini *et al.* [12] suggested this non-coincidence is a *Re* dependent phenomenon and argued that y_U may lag behind y_{uv} in following variations with change of *Re* number. However, this argument does not agree with the previous experimental results, e.g., Lawn & Elliot [6] and Rehme [7]. There is still no clear understanding on the possibility and the cause of non-coincidence which requires further investigation of turbulent mechanisms at the midsection of the annulus.

The present work aims at detailed experimental investigation of the location of y_u and y_{uv} in a high *Re* annular flow facility using particle image velocimetry (PIV) and particle tracking velocimetry (PTV). The experimental investigation also scrutinizes the structure of the turbulent flow at the midsection of the annulus where the two dissimilar boundary layers interact. The profiles of average streamwise velocities and turbulent intensities are investigated in section 3 to specify the location of the extremums at the midsection of the annular gap. Further investigation of the turbulent structures at the midsection of the annuli is provided by the analysis of turbulent fluctuations of the four quadrants [22], turbulent transport, and budget of Reynolds stresses.

II. EXPERIMENTAL SETUP

The experiments are conducted in a flow loop driven by a centrifugal pump equipped with a variable frequency drive to control the flow rate. The pump inlet is fed from a 600 liters mixing tank and the outlet is connected to a 50.8 mm (2" pipe). The test section of the annulus is 9 meters long and is located on the return route of the loop after a short vertical section as shown in Figure 2. The annulus is formed

by two concentric glass tubes. The smaller inner tube has an outer diameter of $2r_1 = d_1 = 38$ mm and the large outer tube has an inner diameter of $2r_2 = d_2 = 95$ mm giving an annular ratio of $d_1/d_2 = 0.4$ and hydraulic diameter of $d_h = 57$ mm. The annular section is constructed from 6 segments each 1.5 meters long which are smoothly connected by stainless steel joints. The wall thickness of the inner tube is selected to provide a buoyant inner tube in water and minimize deflection and vibration effects. The inner tube is held in place at the joints using three threaded rods spaced 120° apart. Measurements are conducted at five bulk velocities (U_b, average velocity over the cross section) presented in Table I along with the corresponding *Re* numbers ($Re = U_b\ d_h / \nu$). The reference point of the radial coordinate y is defined at the outer surface of the inner tube (see Figure 1) and is normalized based on the annulus gap according to

$$y = \frac{r - r_1}{r_2 - r_1}. \tag{3}$$

Flow measurements are carried out using both PIV and PTV techniques. The PIV technique has a lower imaging magnification to investigate the turbulent field across the annular gap while the PTV technique has a higher imaging magnification for high-spatial resolution measurement in the midsection. The spatial resolution of the PIV technique is limited by the number density of the tracer particles. However, PIV has the advantage of instantaneous velocity measurement over a structured grid, which allows estimation of vorticity and spatial correlation. The measurements are carried out at $L = 5.5$ m downstream of the start of the annulus section ($L / d_h = 97$) and one meter downstream of the closest joint holding the threaded rods. As it is shown in Figure 3, the test section is submerged in a rectangular box made of cast-acrylic and filled with glycerol to reduce image distortion due to the pipe curvature. Streamwise and radial velocities are specified by $(U_1, U_2) = (U, V)$ while their fluctuating component is denoted by $(u_1, u_2) = (u, v)$, respectively.

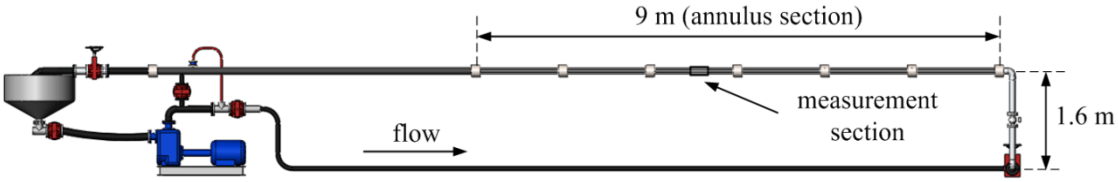

FIG. 2. A schematic of the flow loop and the annulus section formed by two concentric tubes.

TABLE I. Experimental condition including Reynolds number, maximum velocity and bulk average velocity (U_b).

Case	1	2	3	4	5
$Re_b = U_b d_h / \nu$	59200	67000	75000	83000	91000
U_{max} (m/s)	0.934	1.056	1.178	1.300	1.419
U_b (m/s)	0.793	0.899	1.005	1.112	1.217
τ_i (N/m^2)	1.86	2.30	2.75	3.30	3.93
τ_o (N/m^2)	1.78	2.26	2.67	3.18	3.81
λ_i (μm)	18.6	16.7	15.3	13.9	12.8
λ_o (μm)	18.9	16.8	15.5	14.2	13.0

The PIV/PTV setup consists of a double cavity Nd-YAG laser (SoloPIV III, New Wave Research) and a CCD camera (Imager Intense, LaVision). The laser produces 50 mJ/pulse and is equipped with a combination of spherical and cylindrical lenses forming an approximately 1 mm thick laser sheet. The CCD sensor has 1376×1040 pixels with a pixel pitch of 6.45μm viewing the laser sheet at 90° angle through a 105mm SLR lens (Sigma).

The magnification of the PIV imaging system is M = 0.277, which results in a digital resolution of 23 μm/pix. The corresponding field-of-view is 32.092×14.180 mm in radial (y) and streamwise (x) direction, respectively. A set of 12,000 double-frame recordings at an approximate acquisition frequency of 10 Hz (cropped sensor) with pulse separations of 340, 320, 300, 270, and 250 μs is acquired for case 1 to 5 of Table I, respectively. The recorded images are processed using a multi-grid cross-correlation algorithm

with window deformation Scarano & Reithmuller [23] in DaVis 8.0 (LaVision GmbH) with final interrogation windows of 32×32 pixels (0.736×0.736 mm equivalent to $0.0129d_h$×$0.0129d_h$) with 75% overlap yielding a vector spacing of 184 μm. The velocity gradients are estimated using a second order central-difference scheme.

The PTV measurement is carried out at M = 0.796 with spatial-resolution of 8.10 μm/pix covering the region around $<U>_{max}$. The corresponding field-of-view is 11.146×5.184 mm in radial (y) and streamwise (x) direction, respectively. This high-magnification experiment is carried out at the experimental condition of Case 3 (Re_b=75,000) to provide further evidence on the location of $<U>_{max}$ and $<uv>$=0 using a higher-spatial resolution measurement technique. The PTV algorithm is developed in MATLAB based on Maas *et al.* [24] and Malik *et al.* [25] to estimate the velocity of the individual seed particles from double-frame images. The initial detection of particles is carried out using an intensity threshold followed by applying a local maximum filter to remove overlapped, out-of-focused, and distorted particles. The peak location of the selected particles is estimated within subpixel accuracy using a Gaussian fit. The average velocity field obtained using PIV is used as a predictor to detect the particle pairs. The PTV results were binned into 48 pixel windows (389 μm, $0.0068d_h$) in the radial direction for statistical convergence. A set of 12,000 double-frame recordings at an approximate acquisition frequency of 5 Hz with pulse separations of 100 μs is acquired for PTV.

The low-magnification PIV images are also processed using the ensemble of correlation technique [26] for high spatial resolution measurement of the average velocity profile in the vicinity of the inner and outer pipe walls. The final window size is 6×6 pixels (0.138×0.138 mm equivalent to $0.0024d_h$×$0.0024d_h$) with 75% overlap yielding a vector spacing of 184 μm. The Clauser chart method [27] is applied to the mean velocity profile to estimate the wall shear stress (τ) and the wall unit (λ) on both the inner wall (denoted by subscript i) and the outer wall (denoted by subscript o) as shown in Table I. This method is based on the assumption that the mean velocity profile follows the universal logarithmic law (κ = 0.41, B = 5) for the annular flow and is independent of the Reynolds number. The measurements of Quarmby

[34], Lawn and Elliott [6], Rehme [7], and Nouri *et al.* [1] and the DNS of Kaneda *et al.* [28] and Boersma & Breugem [4] confirm that the mean velocity profile of the annular flow follows the logarithmic law (κ = 0.41, B = 5) at $d_1/d_2 > 0.2$ on both the inner and outer wall. Deviation from the universal logarithmic law has been observed for $d_1/d_2 < 0.2$ and only on the inner wall. Rehme [7] has observed deviation on the inner wall for $d_1/d_2 = 0.04$ while the mean velocity still followed the universal law on the outer wall. The measurement of Lawn and Elliott [6] also shows that the deviation is present for $d_1/d_2 < 0.176$. Therefore, the universal logarithmic law is valid for the current experiment ($d_1/d_2 = 0.4$) allowing estimation of the inner scales.

The relative size of the spatial resolution of the measurement system to the smallest scales of the turbulent flow can assess the ability of the PIV system to quantify the turbulent statistics. The in-plane spatial resolution of the PIV is equivalent to the window size while the spatial resolution of the PTV system is equal to the size of the binning window. Lavoie *et al.* [29] evaluated the ability of the PIV measurement in grid turbulence relative to the Kolmogorov length scale (η) estimated by $\nu^{3/4}\langle\varepsilon\rangle^{1/4}$. In this length scale, ν is kinematic viscosity and $\langle\varepsilon\rangle$ is the decay of turbulent kinetic energy available through theory and DNS of grid turbulence. They have suggested an interrogation window of 5η for the estimation of the small scale statistics with 30% accuracy. In a turbulent boundary layer, Stanislas *et al.* [30] have shown that the smallest coherent structures with a life time long enough to contribute to the turbulent statistics are approximately 20λ. This length scale is equivalent to 370, 330, 300, 280, 260μm for Case 1 to 5 of Table 1, respectively.

The ratio of the spatial resolution of the PIV to the smallest coherent length scale ($l = 20\lambda$) is 2.0, 2.2, 2.4, 2.6, and 2.9 for Case 1 to 5 of Table 1, respectively. The spatial resolution of the PTV system is 1.0, 1.2, 1.3, 1.4, and 1.5 for Case 1 to 5, respectively. Saikrishnan *et al.* [31] applied a spatial filter on DNS data to simulate the effect of finite window size on measurement turbulent fluctuations and vorticity vector using PIV. Their results show that a window size of 50λ (corresponding to current PIV measurement at Case 3) captures about 80% and 95% of turbulent fluctuations ($\langle u^2\rangle$, $\langle v^2\rangle$, and $\langle w^2\rangle$) in

the logarithmic region (y^+=110) and the outer region (y/δ = 0.5), respectively. A window size of 25λ (corresponding to current PTV measurement at Case 3) captures about 92% and 98% of turbulent fluctuations ($\langle u^2 \rangle$, $\langle v^2 \rangle$, and $\langle w^2 \rangle$) in logarithmic region (y^+=110) and the outer region (y/δ = 0.5), respectively. The underestimation reduced with increase of wall normal distance since the population of small scale turbulent fluctuations decreases. Saikrishnan *et al.* [31] also evaluated the effect of spatial filter on calculating the vorticity vector which includes spatial derivatives. With a spatial filter of 50λ about 70% of the vorticity vector is captured at y/δ = 0.5. In the current experiment, both PIV and PTV demonstrate enough spatial resolution to capture the turbulent statistics with no spatial gradient. The turbulent statistics which include spatial gradient are prone to underestimation due to finite size of the PIV interrogation window.

FIG 3. The PIV/PTV setup consists of a camera imaging perpendicular to the laser sheet. The test section of the flow loop is contained in a glycerol box minimizing distortion effects caused by the round glass pipe.

III. LOCATION OF y_U and y_{uv}

Average streamwise and radial velocities normalized by the maximum streamwise velocity ($\langle U \rangle_{max}$) for the Reynolds numbers of Table I are shown in Figure 4(a). The normalized profiles of $\langle U \rangle$ overlap across the annual gap except at a narrow region in the vicinity of the walls where inner wall scaling should be applied. The profiles are skewed and $\langle U \rangle_{max}$ is closer to the inner wall. The smaller surface

area of the inner wall exerts a smaller friction force on the fluid relative to the outer wall, which results in higher velocity in the vicinity of the inner wall. The profiles of average radial velocity in Figure 4(a) also show that the $\langle V \rangle$ is not zero. However, the average value over the annular gap (V_b) is in the range of 0.003-0.005 m/s for all the *Re* numbers which is three orders of magnitude smaller than U_b.

The profiles of normal and Reynolds shear stress normalized using $\langle U \rangle_{max}$ (outer scaling) are shown in Figure 4(b). The profiles are asymmetric and overlap at different *Re* numbers while they are skewed towards the inner wall. The locations of $\langle u^2 \rangle_{min}$, $\langle v^2 \rangle_{min}$, and $\langle uv \rangle = 0$ in the midsection are closer to the inner wall and at about $y = 0.45$. In the vicinity of the walls, the local maximum of $\langle v^2 \rangle$ is at $y = 0.09$ and 0.83 while the exact location of maximum $\langle u^2 \rangle$ is not visible due to the lack of near wall data. The radial gradient of turbulent intensities $\partial \langle u^2 \rangle / \partial y$ and $\partial \langle v^2 \rangle / \partial y$ are steeper in the vicinity of the inner wall due to the thinner boundary layer. In addition, the local maximum of $\langle v^2 \rangle$ at $y = 0.09$ is larger than the local maximum at $y = 0.83$ which suggests more intense fluctuations at the inner wall boundary layer. The profile of Reynolds shear stress is slightly non-linear in the middle of the annulus which is in agreement with the previous experimental observations of Rehme [21] and Jung & Sung [31]. The numerical simulations have shown that the deviation from the linear distribution is a function of r_1/r_2 [3, 4, 28].

The profiles in the vicinity of $\langle U \rangle_{max}$, $\langle uv \rangle = 0$, $\langle u^2 \rangle_{min}$ and $\langle v^2 \rangle_{min}$ at the midsection of the annular gap are shown in the magnified views of Figure 5 and summarized in Figure 6. The statistical convergence of the average values is investigated in the Appendix section. The maximum streamwise velocity $\langle U \rangle_{max}$ is at $y = 0.456$ for the first four Reynolds number and slightly shifts to $y = 0.450$ for the highest Reynolds number in Figure 5(a). In general, a slight shift of the profile towards the inner wall is observed with increase of *Re*. The displacement is relatively small (about $\Delta y = 0.006$) showing that y_U location has reached its asymptotic location with increase of *Re*. The $\langle uv \rangle$ profile of Figure 5(b) shows an opposite slight shift towards the outer wall with increase of Reynolds number. However, $y_U - y_{uv}$ is positive within the investigated *Re* showing a systematic non-coincidence. The minimum separation of $y_U - y_{uv}$ is 0.0062 for *Re* = 90,800 and the maximum separation is 0.0186 for *Re* = 59,200 and 83,000 based

on the PIV measurement. The non-coincidence is not only limited to y_U and y_{uv}. The locations of $<u^2>_{min}$ and $<v^2>_{min}$ in Figure 5(c) and (d) are also apart from y_U and appear to be closer or overlap with y_{uv} as illustrated in Figure 6.

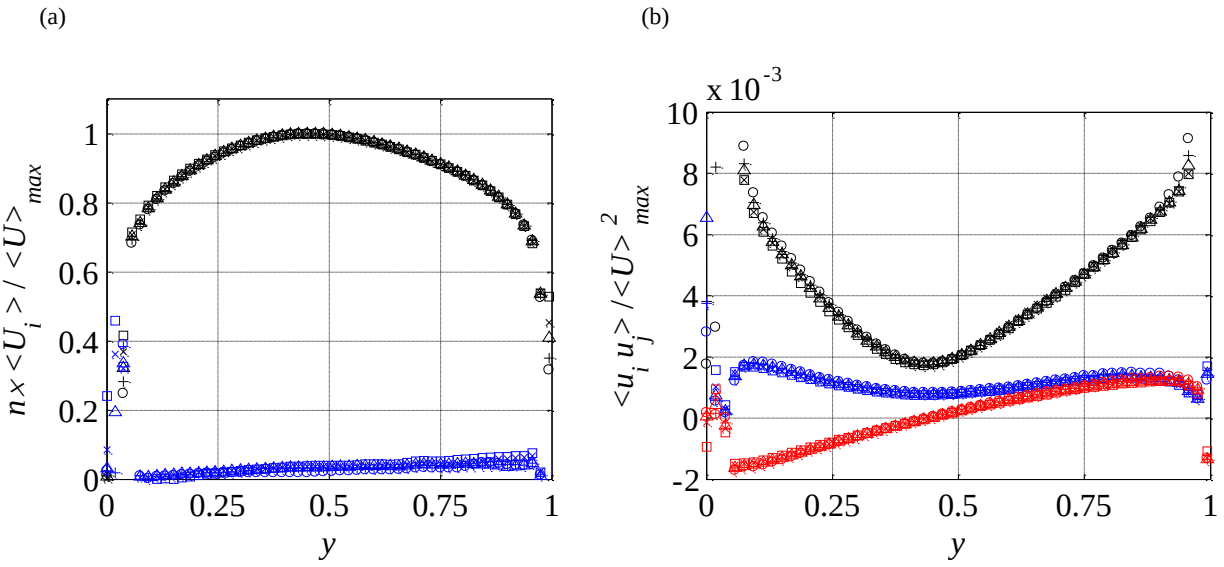

FIG. 4. Profiles of (a) average streamwise velocity $U_1 = <U>/<U>_{max}$ (upper) and radial velocity $U_2 = 10\times<V>/<U>_{max}$ (lower), and (b) $<u_1u_1> = <u^2>$ (upper in black), $<u_2u_2> = <v^2>$ (middle in blue), $<u_1u_2> = <uv>$ (lower in red) across the annular gap. Symbols: o, Re_b = 59,200; +, Re_b = 67000; Δ, Re_b = 75,000; ×, Re_b = 83,000; □, Re_b = 90,800. One out of every three data points is shown for clarity.

Burattini *et al.* [12] hypothesized in their investigation of asymmetric channel flow that the non-coincidence of y_U and y_{uv} might be due to slower variation of first-order quantities (y_U) relative to second-order quantities (y_{uv}) with variation of Reynolds number. They argued that at high enough Reynolds number y_U and y_{uv} may converge. However, the current and previous experimental investigations do not show such a trend. Measurements of Lawn & Elliott [6] in an annular tube with $r_1/r_2 = 0.396$ shows the normalized distance of y_U and y_{uv} to be almost constant and approximately equal to $\Delta y \approx 0.008$ for Re_b of 30,000 to 150,000. The measurements of Rehme [7] in an annular pipe with a larger degree of asymmetry (due to small $r_1/r_2 = 0.1$) also shows relatively constant Δy of 0.033 over Re_b range of 20,000 to 200,000. At lower Reynolds numbers of 8,900 to 26,600, Nouri *et al.* [1] reported small and non-distinguishable

distance within their measurement uncertainty, which also does not support the conjecture of smaller y_U - y_{uv} at high *Re* number.

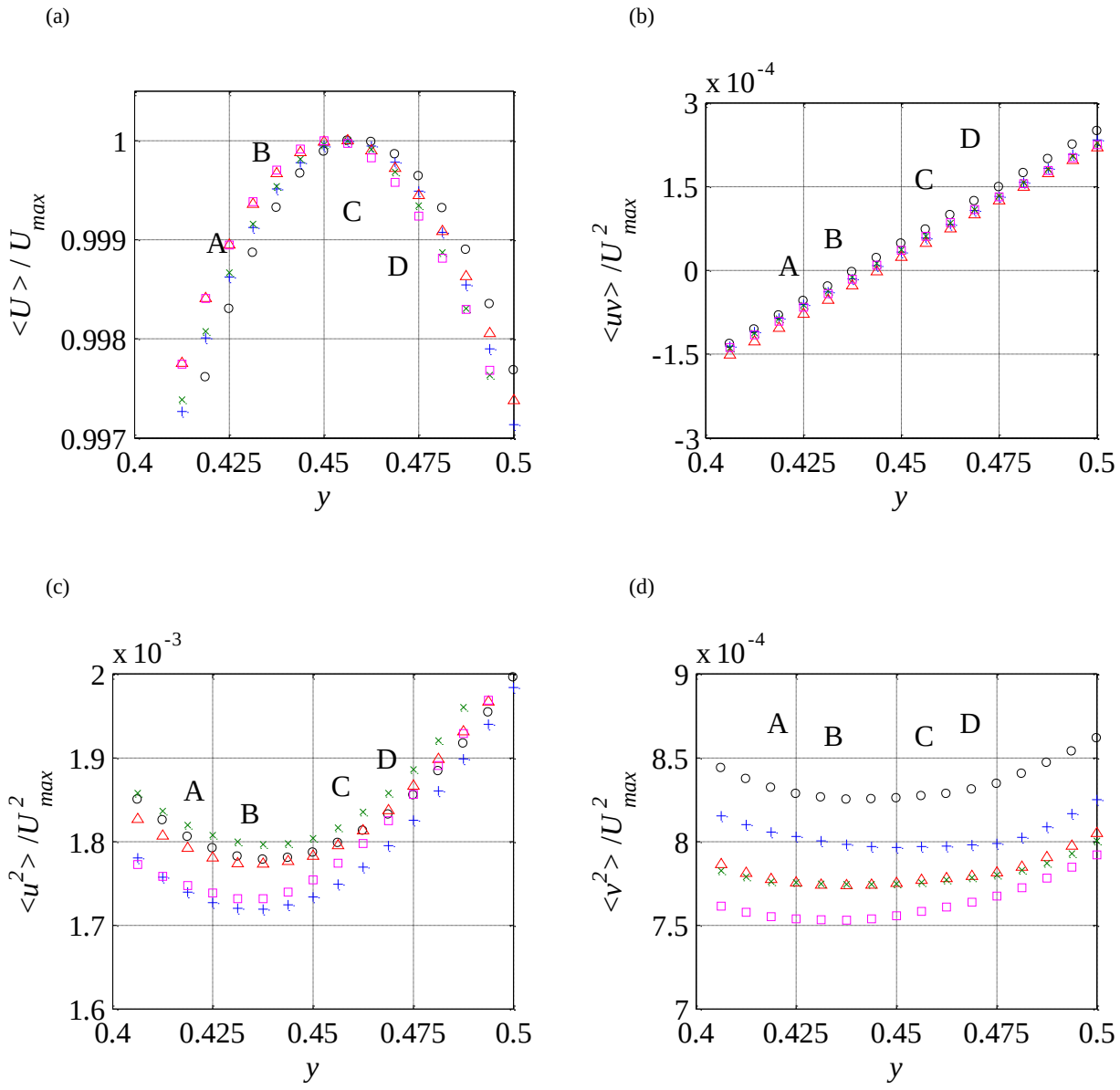

FIG. 5. Profiles of (a) < U > (b) < uv >, (c) < u^2 >, (c) and < v^2 > at the midsection of the annular gap. Symbols similar to fig. 4.

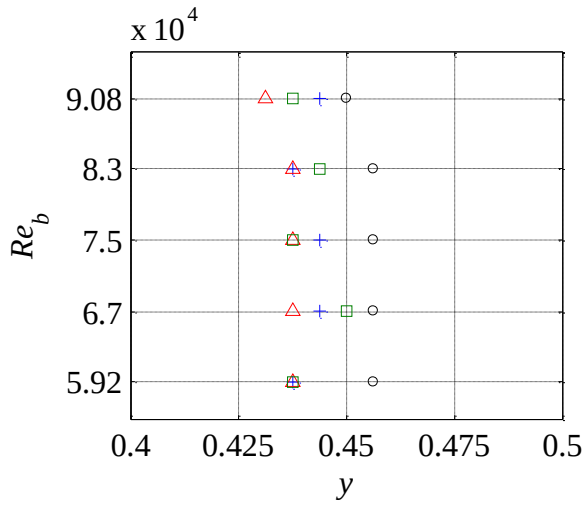

FIG. 6. The location of $<U_{max}>$, $<uv> = 0$, $<u^2>_{min}$, and $<v^2>_{min}$ versus Reynold's numbers shown by o, +, Δ, and □ symbols, respectively.

The PTV with high digital resolution is applied to further investigate the location of $<U>_{max}$, $<uv> = 0$, $<u^2>_{min}$ and $<v^2>_{min}$ at the midsection of the annulus at Re = 75,000. The velocity of the individual tracer particles are binned into 48 pixel windows (no overlap) for statistical convergence and shown in Figure 7. The final spatial resolution of the current PTV measurement is half of the PIV. The results shows that $y_U - y_{uv}$ are $0.013d_h$ apart. The locations of $<u^2>_{min}$ and $<v^2>_{min}$ also do not overlap with $<U>_{max}$ and $<uv> = 0$. The PTV results confirm the non-coincidence of y_{uv} and the extremums while also showing underestimation of the separation distances by the PIV measurement.

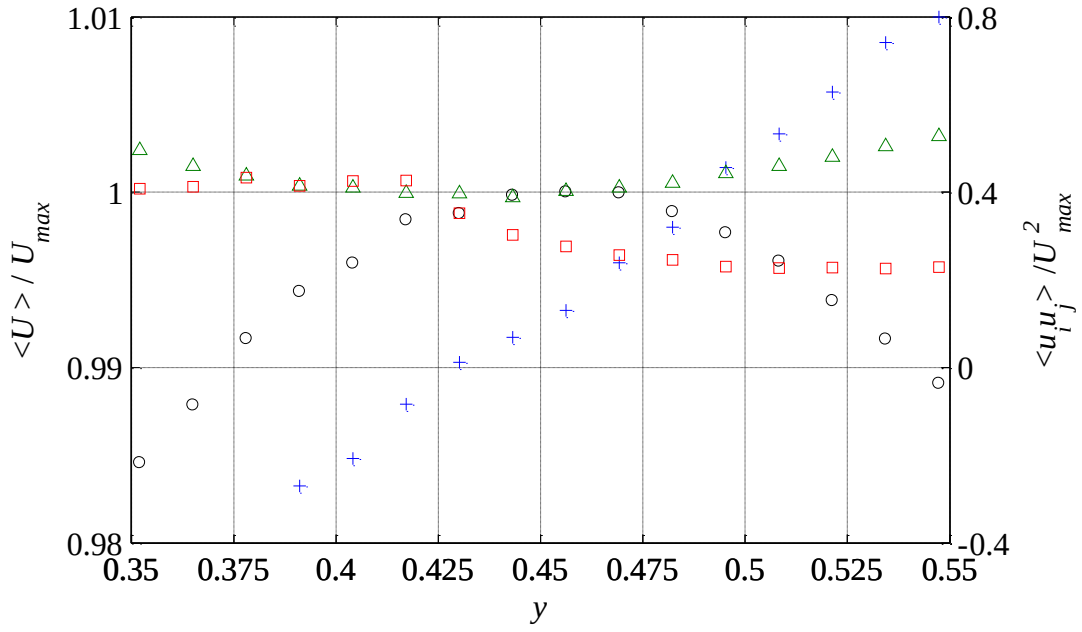

FIG. 7. Profiles of $< U >$ (right vertical axis) and $<uv>$, $< u^2 >$, and $< v^2 >$ (left vertical axis) at the midsection of the annular gap from PTV averaged over 48 pixel windows. The symbols similar to fig. 6.

IV. THE TURBULENT STRUCTURE AT THE ANNULUS MIDSECTION

The structure of turbulent fluctuations in the vicinity of $<U>_{max}$, $<u^2>_{min}$, $<v^2>_{min}$, and $<uv> = 0$ is investigated here to reveal the interaction of the inner and outer wall flows at the midsection of the annuli and explain the non-coincidence of these points. Since the profiles of Figure 4 and 5 for different Reynolds numbers were similar, the analysis of this section is limited to a single case of Table I (case 4 at Re_b = 83,000). The analysis is carried out using PIV data due to instantaneous measurement of flow field on a structured grid of data allowing estimation of spatial derivatives and correlations.

A. Quadrant analysis

In the *x*-*y* coordinate system of Figure 8, the ejection and sweep events of the inner wall flow occur at the typical *Q*2 and *Q*4 quadrants while the ejection and sweep events of the outer wall flow occur at *Q*3 and *Q*1 quadrants, respectively. The dominance of the ejection and sweep events of each wall and their sign reversal can help to identify the extent of each boundary layer across the annular gap. For this

purpose, the contribution of the fluctuations of each quadrant to the shear and normal Reynolds stresses is investigated using conditional averaging based on the quadrant of u and v fluctuations expressed as

$$\langle u_i u_j \rangle_k = \langle u_i u_j \rangle \big| (u_i, u_j) \in Q_k \tag{4}$$

In which i =1:2 ($u_1 = u$ and $u_2 = v$), and k = 1:4 specifies the quadrant of the turbulent fluctuations based on the v versus u plot similar to the schematic in Figure 8.

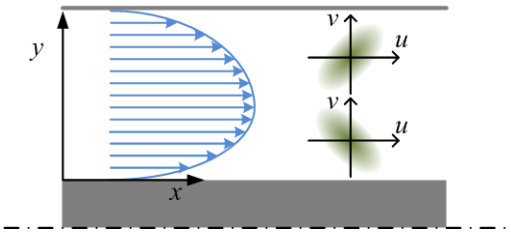

FIG. 8. A schematic view of turbulent fluctuation of the inner and outer wall with respect to the quadrants of the y-x coordinate system.

The conditional averages of $\langle uv \rangle$, $\langle u^2 \rangle$ and $\langle v^2 \rangle$ based on the quadrants are shown in Figure 9, 10, and 11, respectively. The ejection of $Q2$ quadrant ($\langle uv \rangle_2$) and the sweep events of $Q4$ quadrant ($\langle uv \rangle_4$) dominant the turbulent fluctuations in the vicinity of the inner wall as observed in Figure 9(a). The intensity of $\langle uv \rangle_2$ and $\langle uv \rangle_4$ reduces with increase of y till a minimum is reached at y = 0.525 for $\langle uv \rangle_2$ and at y = 0.475 for $\langle uv \rangle_4$. Both minimums are beyond $\langle U \rangle_{max}$ (y_U = 0.456) and $\langle uv \rangle$ = 0 (y_{uv} = 0.438) locations. In the vicinity of the outer wall, the dominant fluctuations are the ejection of $Q3$ quadrant ($\langle uv \rangle_3$) and the sweep events of $Q1$ quadrant ($\langle uv \rangle_1$), respectively. The minimum of $\langle uv \rangle_3$ is at y = 0.3250 and the minimum of $\langle uv \rangle_1$ is at y = 0.3937 which are also further away from the outer wall in comparison to y_U and y_{uv} locations. This extension of the ejection and sweep events of each wall beyond the y_U location shows that the two boundary layers strongly merge into each other at the midsection. This overlap region is approximately $\Delta y \approx 0.19$ wide based on the distance between minimums of $\langle uv \rangle_2$ and $\langle uv \rangle_3$ (ejections) or $\Delta y \approx 0.13$ based on the distance between minimums of $\langle uv \rangle_1$ and $\langle uv \rangle_4$ (sweeps).

The magnified view of Figure 9(b) shows that the conditional average of the ejection events of the inner wall $<uv>_2$ becomes equal to the ejection events of the outer wall $<uv>_3$ at y = 0.4375. At this location, the sweep events of the inner wall $<uv>_2$ and the sweeps of the outer wall also cancel out. The combination results in coincidence with y_{uv}.

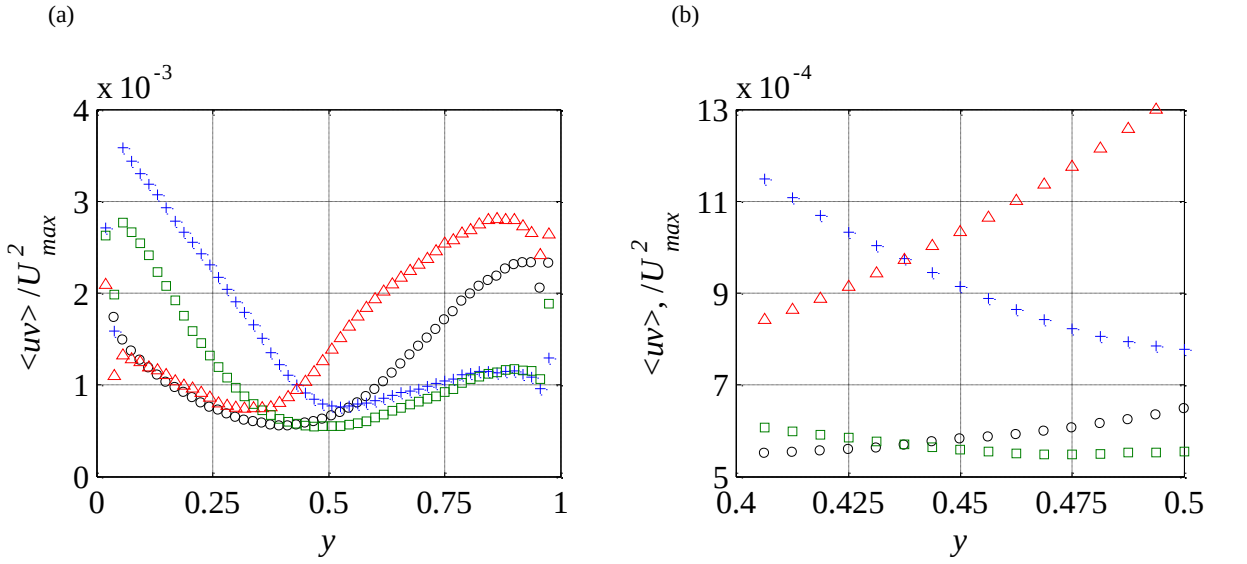

FIG. 9. Conditional averaging of Reynolds shear stress $<uv>$ (a) across the annular gap (one out of every three data points is shown for clarity), and (b) the magnified view at the centerline region. Symbols show conditional averaging based on: o, $Q1$; +, $Q2$; Δ, $Q3$; □, $Q4$.

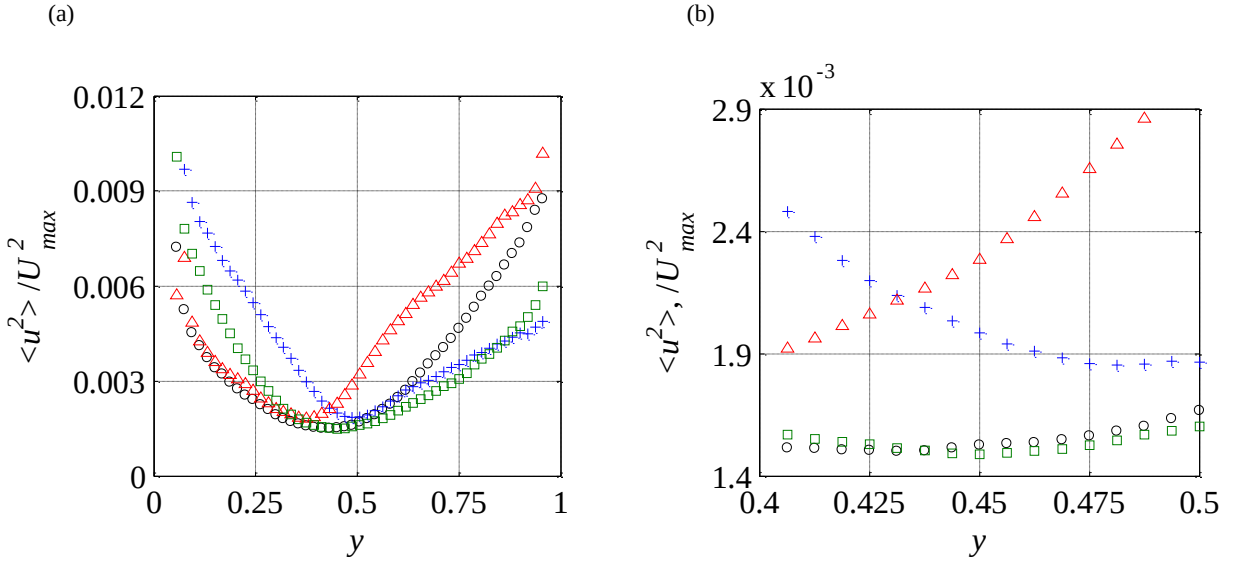

FIG. 10. Conditional averaging of Reynolds shear stress $<u^2>$ (a) across the annular gap, and (b) the magnified view at the centerline region. Symbols similar to figure 9.

The conditional averages of normal Reynolds stresses $\langle u^2 \rangle$ and $\langle v^2 \rangle$ are shown in Figure 10 and 11. In both figures, $Q2$ and $Q4$ events dominate the inner wall vicinity while $Q3$ and $Q1$ dominate the outer wall region. The location of minimum values of $\langle u^2 \rangle_2$, $\langle u^2 \rangle_4$, $\langle v^2 \rangle_2$, and $\langle v^2 \rangle_4$ are larger than y_U and y_{uv} locations and closer to the outer wall. On the other hand, the location of the minimum values of $\langle u^2 \rangle_3$, $\langle u^2 \rangle_1$, $\langle v^2 \rangle_3$, and $\langle v^2 \rangle_1$ events are on the inner wall side of y_U and y_{uv}. The magnified views of Figure 9(b) and 10(b) also demonstrate that the normal Reynolds stresses of the opposing ejection events ($Q2$ versus $Q3$) and the opposing sweep events ($Q1$ versus $Q4$) of the inner and outer walls cancel out in the vicinity of y_{u2} (minimum $\langle u^2 \rangle$), y_{v2} (minimum $\langle v^2 \rangle$) and also y_{uv}, which is further away from y_U.

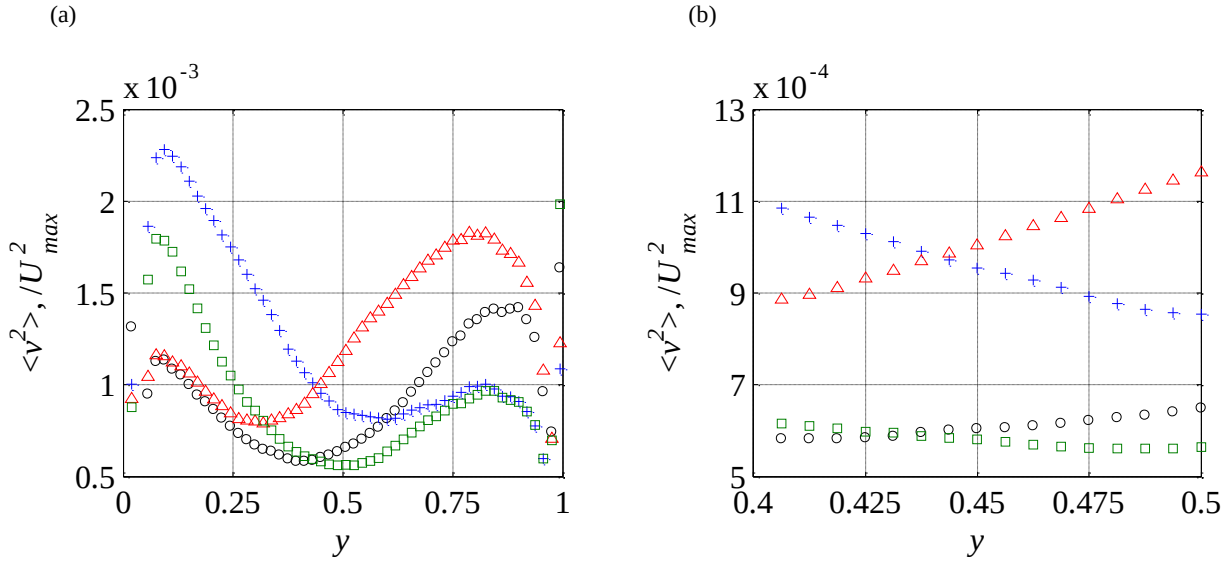

FIG. 11. Conditional averaging of Reynolds shear stress $\langle v^2 \rangle$ (a) across the annular gap, and (b) the magnified view at the centerline region. Symbols similar to figure 8.

B. Transport of turbulence

The transport of turbulent kinetic energy is evaluated to investigate the mechanisms influencing the location of $\langle u^2 \rangle_{min}$, $\langle v^2 \rangle_{min}$, and $\langle uv \rangle = 0$. The transport direction of $\langle u^2 \rangle$ is characterized by investigating the triple products of $\langle uu^2 \rangle$ and $\langle vu^2 \rangle$ in Figure 12 showing that $\langle uu^2 \rangle$ is negative across the annuli while $\langle vu^2 \rangle$ changes from positive to negative with increase of y. The magnified view of Figure 12(b) shows that the local maximum of $\langle uu^2 \rangle$ in the centerline region of the annulus is at y = 0.425 and the sign change of $\langle vu^2 \rangle$ occurs at y = 0.431. As a result, transport of $\langle u^2 \rangle$ is dominated by

ejection events of the inner wall ($u < 0$ and $v > 0$) at $y < 0.431$ and dominated by the ejection events of the outer wall ($u < 0$ and $v < 0$) at $y > 0.431$. The transport of $\langle v^2 \rangle$ in Figure 13 is observed to be through $u < 0$ fluctuations across the channel. The radial fluctuation v changes from positive to negative at $y = 0.438$. The combination shows that $\langle v^2 \rangle$ is on average transported by ejections of the inner and outer walls.

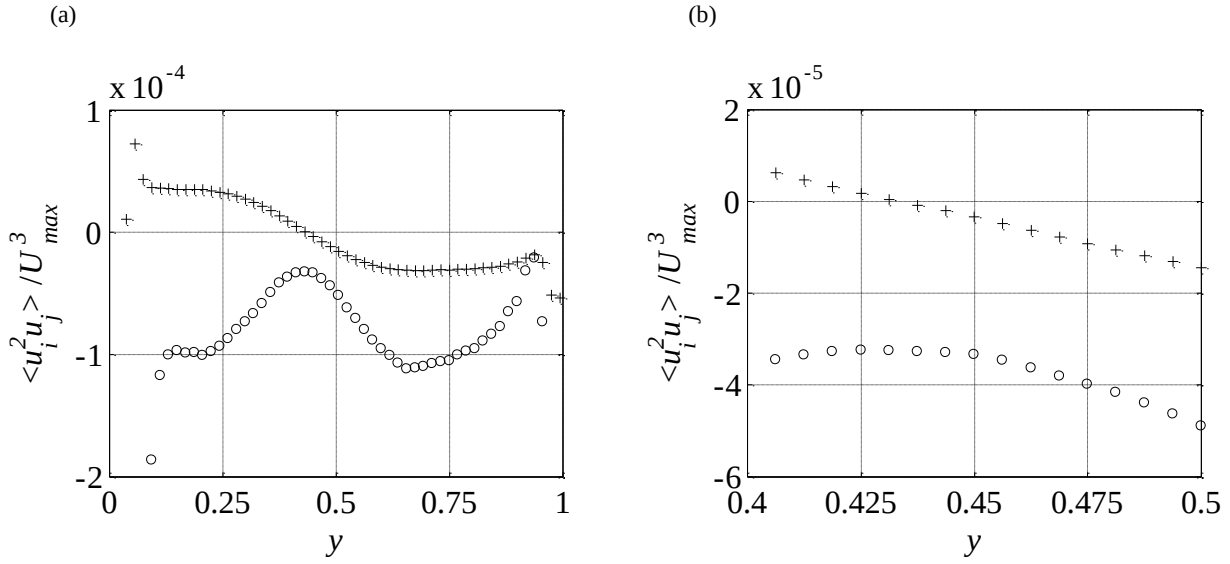

FIG. 12. Turbulent transport by $\langle uu^2 \rangle$ and $\langle vu^2 \rangle$ (a) across the annulus and (b) the magnified view of the centerline region. Symbols: o, $\langle uu^2 \rangle$; + $\langle vu^2 \rangle$.

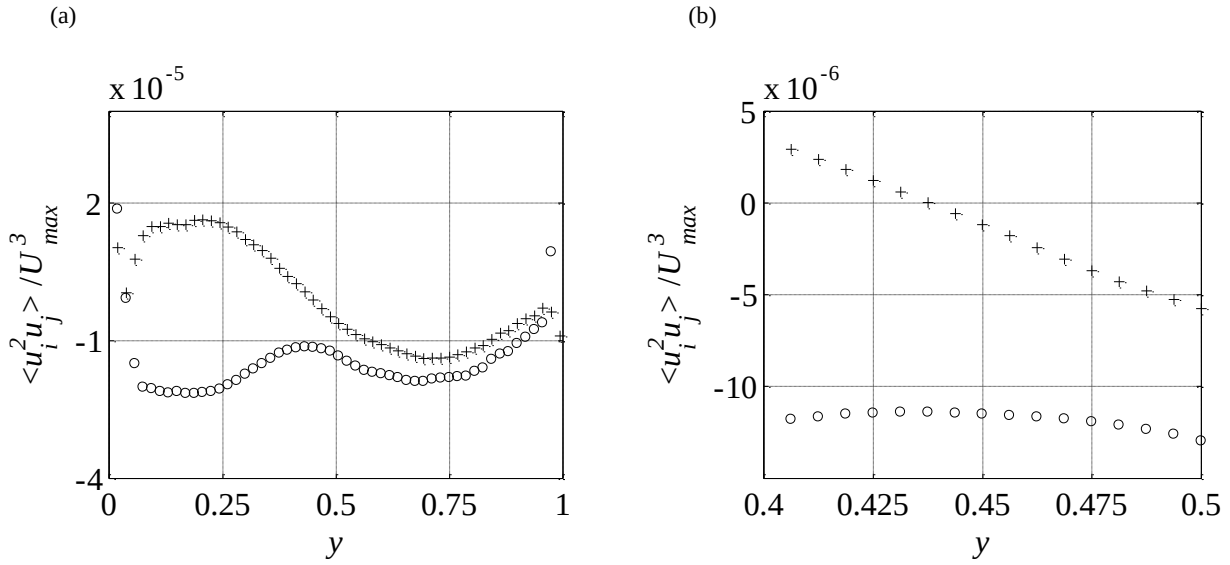

FIG. 13. Turbulent transport by $\langle v^3 \rangle$ and $\langle uv^2 \rangle$ (a) across the annulus and (b) the magnified view at the centerline. Symbols: o, $\langle uv^2 \rangle$; + $\langle vv^2 \rangle$.

C. Budget of Reynolds stresses

The budget of normal and shear Reynolds stresses is investigated to identify the contribution of different mechanisms to the locations of $\langle u^2 \rangle_{min}$, $\langle v^2 \rangle_{min}$, and $\langle uv \rangle = 0$. The budget term and its effect on the locations is investigated. The transport equation of Reynolds stress is obtained based on the Navier-Stokes equation and is given by

$$A_{ij} + P_{ij} + T_{ij} + D_{ij} + \Pi_{ij} + \epsilon_{ij} = 0 \tag{5}$$

where

Advection: $$A_{ij} = -\frac{D}{Dt}\langle u_i u_j \rangle \tag{6}$$

Production: $$P_{ij} = -\langle u_i u_k \rangle \frac{\partial \langle U_j \rangle}{\partial x_k} - \langle u_j u_k \rangle \frac{\partial \langle U_i \rangle}{\partial x_k} \tag{7}$$

Turbulent transport: $$T_{ij} = -\frac{\partial}{\partial x_k}\langle u_i u_j u_k \rangle \tag{8}$$

Viscous diffusion: $$D_{ij} = \nu \nabla^2 \langle u_i u_j \rangle \tag{9}$$

Velocity pressure-gradient: $$\Pi_{ij} = -\frac{1}{\rho}\langle u_i \frac{\partial p}{\partial x_j} + u_j \frac{\partial p}{\partial x_i} \rangle \tag{10}$$

Dissipation: $$\epsilon_{ij} = -2\nu \langle \frac{\partial u_i}{\partial x_k} \frac{\partial u_j}{\partial x_k} \rangle \tag{11}$$

This equation is simplified for the annular flow assuming stationary flow ($\partial/\partial t = 0$ for average quantities), negligible $\partial/\partial z$ of average quantities (azimuthal gradient) and $\langle W \rangle = 0$. The small radial velocity (V) observed in Figure 4(a) is not neglected in this analysis to scrutinize any deviation from the fully developed state. All the terms are available from the PIV data except the velocity pressure-gradient term (equation 10) and the $\langle \partial/\partial z \rangle$ components of dissipation (equation 11). The budget of Reynolds shear stress $\langle uv \rangle$ becomes

Advection: $$A_{12} = -\langle V \rangle \frac{\partial \langle uv \rangle}{\partial y} \quad (12)$$

Production: $$P_{12} = -\langle uv \rangle \frac{\partial \langle U \rangle}{\partial x} - \langle v^2 \rangle \frac{\partial \langle U \rangle}{\partial y} - \langle u^2 \rangle \frac{\partial \langle V \rangle}{\partial x} - \langle uv \rangle \frac{\partial \langle V \rangle}{\partial y} \quad (13)$$

Turbulent transport: $$T_{12} = -\frac{\partial}{\partial y}\langle uv^2 \rangle - \frac{\partial}{\partial x}\langle u^2 v \rangle \quad (14)$$

Viscous diffusion: $$D_{12} = \nu \frac{\partial^2 \langle uv \rangle}{\partial x^2} + \nu \frac{\partial^2 \langle uv \rangle}{\partial y^2} \quad (15)$$

Dissipation: $$\epsilon_{12} = -2\nu \left(\langle \frac{\partial u}{\partial x} \frac{\partial v}{\partial x} \rangle + \langle \frac{\partial u}{\partial y} \frac{\partial v}{\partial y} \rangle + \langle \frac{\partial u}{\partial z} \frac{\partial v}{\partial z} \rangle \right) \quad (16)$$

The first and the forth terms of equation 13 cancel out following the continuity equation ($\partial\langle U\rangle/\partial x + \partial\langle V\rangle/\partial y = 0$). The third term is also neglected in comparison to the second term since $\partial/\partial x < \partial/\partial y$ and $\langle V\rangle$ is also three orders of magnitude smaller than $\langle U\rangle$. The second term of the equation 14 and the first term of the equation 15 are neglected due to small streamwise gradient. The profiles of the budget terms following equations 12 to 16 are non-dimensionalized by $\langle U\rangle_{max}^4/\nu$ and presented in Figure 14. The positive values are denoted by "Gain" while negative values are presented as "Loss" of the Reynolds stress. The advection of Reynolds shear stress (equation 12) is present due to the small radial velocity across the annular gap. This term decreases with distance from the wall and is negative and rather flat at the midsection of the annulus as shown in Figure 14. The negative advection is in favor of the negative $\langle uv\rangle$ of the inner wall ($y < y_{uv}$) while it opposes the positive $\langle uv\rangle$ of the outer wall side. The production term is observed to be significantly larger than the other terms and is expected to be mainly balanced out by the velocity pressure-gradient term similar to a turbulent channel flow [32]. The turbulent transport term has a negative local minimum at $y = 0.319$ and a positive local maximum at $y = 0.525$ where it makes the highest contributions to the local $\langle uv\rangle$. The viscous diffusion term is significantly smaller than other terms and has a flat profile due to the relatively linear distribution of $\langle uv\rangle$ at the midsection of the annulus. The small value of diffusion does not agree with Rehme [21] conjecture that diffusion of

turbulence is large for asymmetric profiles causing the non-coincidence. The positive dissipation works against the negative $\langle uv \rangle$ of $y < 0.4375$ while the negative dissipation counteracts the positive distribution of $\langle uv \rangle$ at $y > 0.4375$.

The variation in the terms of the $\langle uv \rangle$ budget is of interest at the point of $\langle U \rangle_{max}$ ($y_U = 0.4562$) and $\langle uv \rangle = 0$ ($y_{uv} = 0.4375$) as shown in the magnified view of Figure 14(b). At y_U, the production and dissipation terms become zero. This is expected for the production term since the dominant term (the second term of equation 13) becomes zero at $\partial \langle U \rangle / \partial y = 0$. However, the observed coincidence of zero dissipation with y_U is not trivial from equation 16. It is important to note that the third term of equation 16 is not available through planar PIV. At y_{uv}, the advection and production terms are negative while the dissipation term is positive. A hypothetical stronger advection or production term with a larger negative value at this point would shift the $\langle uv \rangle$ profile downwards and toward negative values. As a result, the y_{uv} location would move towards y_U. In contrary, a hypothetical stronger dissipation with a larger positive value at this point would shift y_{uv} away from y_U. Therefore, the production and advection terms acts towards the coincidence of y_U and y_{uv} while the dissipation terms would move them further apart. The turbulent transport term becomes zero at y_{uv} and is not expected to directly influence the location of y_{uv}. The coincidence of zero turbulent transport term with y_{uv} is expected since $\langle uv^2 \rangle$ reaches its local maximum at this point as it was observed in Figure 13.

(a) (b)

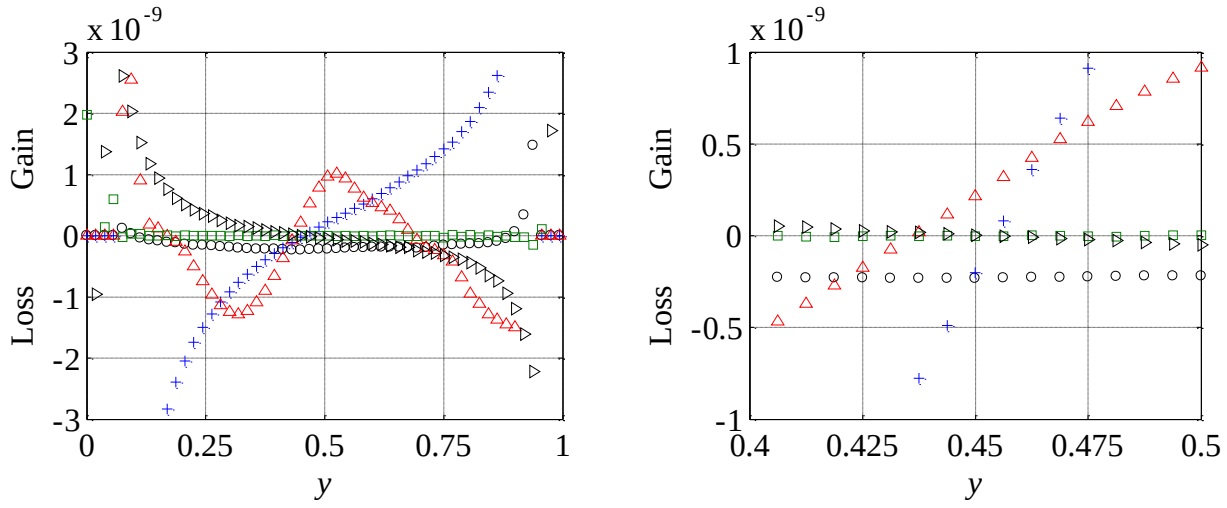

FIG. 14. Budget of Reynolds shear stress <*uv*> (a) across the annulus and (b) the magnified view at the centerline. Symbols: o, A_{12}; +, P_{12}; Δ, T_{12}; □, D_{12}; ▷ , ε_{12}.

The budget of Reynolds normal stresses is of interest to investigate the non-coincidence of $\langle U\rangle_{max}$ and $\langle u^2\rangle_{min}$ and $\langle v^2\rangle_{min}$. The budget of streamwise Reynolds normal stress $\langle u^2\rangle$ follows

Advection: $$A_{11} = -\langle V\rangle \frac{\partial \langle u^2\rangle}{\partial y} \tag{17}$$

Production: $$P_{11} = -2\langle u^2\rangle \frac{\partial \langle U\rangle}{\partial x} - 2\langle uv\rangle \frac{\partial \langle U\rangle}{\partial y} \tag{18}$$

Turbulent transport: $$T_{11} = -\frac{\partial}{\partial x}\langle u^3\rangle - \frac{\partial}{\partial y}\langle vu^2\rangle \tag{19}$$

Viscous diffusion: $$D_{11} = \nu \frac{\partial^2 \langle u^2\rangle}{\partial x^2} + \nu \frac{\partial^2 \langle u^2\rangle}{\partial y^2} \tag{20}$$

Dissipation: $$\epsilon_{11} = -2\nu \left(\langle \frac{\partial u}{\partial x}\frac{\partial u}{\partial x}\rangle + \langle \frac{\partial u}{\partial y}\frac{\partial u}{\partial y}\rangle + \langle \frac{\partial u}{\partial z}\frac{\partial u}{\partial z}\rangle \right) \tag{21}$$

And the budget of Reynolds radial normal shear stress $\langle v^2\rangle$ is

Advection: $$A_{22} = -\langle V\rangle \frac{\partial \langle v^2\rangle}{\partial y} \tag{22}$$

Production: $$P_{22} = -2\langle uv \rangle \frac{\partial \langle V \rangle}{\partial x} - 2\langle v^2 \rangle \frac{\partial \langle V \rangle}{\partial y} \quad (23)$$

Turbulent transport: $$T_{22} = -\frac{\partial}{\partial x}\langle uv^2 \rangle - \frac{\partial}{\partial y}\langle v^3 \rangle \quad (24)$$

Viscous diffusion: $$D_{22} = \nu \frac{\partial^2 \langle v^2 \rangle}{\partial x^2} + \nu \frac{\partial^2 \langle v^2 \rangle}{\partial y^2} \quad (25)$$

Dissipation: $$\epsilon_{22} = -2\nu \left(\langle \frac{\partial v}{\partial x} \frac{\partial v}{\partial x} \rangle + \langle \frac{\partial v}{\partial y} \frac{\partial v}{\partial y} \rangle + \langle \frac{\partial v}{\partial z} \frac{\partial v}{\partial z} \rangle \right) \quad (26)$$

The first term of equations 18, 19, 20 from $<u^2>$ budget and the first terms of equations 23, 24, and 25 from $<v^2>$ budget are neglected due to smaller streamwise gradient in comparison to the radial gradient. The budget terms of $<u^2>$ and $<v^2>$ are non-dimensionalized by $<U>_{max}^4/\nu$ and shown in Figure 15 and 16 in terms of gain (positive) and loss (negative). The advection of $<u^2>$ and $<v^2>$ has a positive value at the inner wall side ($y < y_{u2}$) and a negative value at the outer wall side ($y > y_{v2}$). This term becomes zero at y_{u2} and y_{v2} as expected from equations 17 and 22 and also observed in the magnified views of Figure 15(b) and 16(b), respectively. The production of $<u^2>$ is larger than other terms in the vicinity of the walls (not fully visible within the vertical axis limits of Figure 15(a)) while it significantly reduces at the midsection of the annular gap. A region of negative production of $<u^2>$ is observed between y_{u2} and y_U although the negative magnitude is rather small. This narrow region of small negative production of $<u^2>$ shows energy transfer from the turbulent fluctuations (u) to the mean streamwise flow ($<U>$). The production of $<v^2>$ is negative at both y_{v2} and y_U locations due to the small positive radial velocity demonstrating transfer of energy from radial velocity fluctuations (v) to radial mean flow ($<V>$). The transport and the dissipation terms are the dominant mechanisms in both budget distributions with a relatively flat distribution between y = 0.4 to 0.5. The diffusion term is also observed to be negligible in this region similar to the budget of $<uv>$.

In general, most of the budget terms of $<u^2>$ and $<v^2>$ are rather constant (small variation between) y_U and y_{uv}, which makes it difficult to conjecture on the most dominant term affecting the location of $<u^2>_{min}$

and $\langle v^2 \rangle_{min}$. The production of turbulent kinetic energy $e = 1/2\langle u_{ii}^2 \rangle$ for a two dimensional ($\langle W \rangle = 0$ and $\partial/\partial z = 0$) and fully developed (assuming both $\partial/\partial x = 0$ and $\langle V \rangle = 0$) flow becomes the same as equation 18 (production of $\langle u^2 \rangle$). Therefore, the production of turbulent kinetic energy is zero at both y_U and y_{uv} and is negative in the region in between them. Eskinazi & Erian [19] have argued that a zone of negative production of turbulence (energy reversal zone) has high rates of diffusion. However, they did not directly measure the diffusion term and did not have access neither to the transport term nor the velocity pressure-gradient term. The high rate of diffusion is not observed in Figures 14, 15 or 16 as all demonstrate rather negligible diffusion values in the mid-section. However, the rate of diffusion is underestimated here due to the limited spatial resolution in calculating the gradients of velocity fluctuations as discussed in section II.

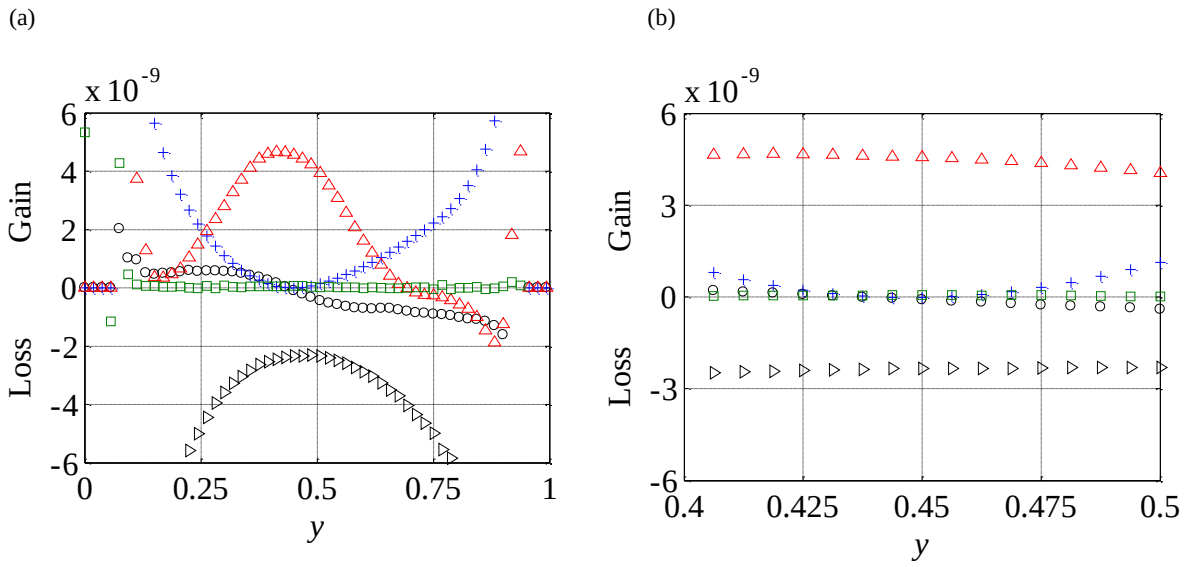

FIG. 15. Budget of Reynolds shear stress $\langle u^2 \rangle$ (a) across the annulus and (b) the magnified view at the centerline. Symbols: o, A_{11}; +, P_{11}; Δ, T_{11}; □, D_{11}; ▷ , ε_{11}.

(a) (b)

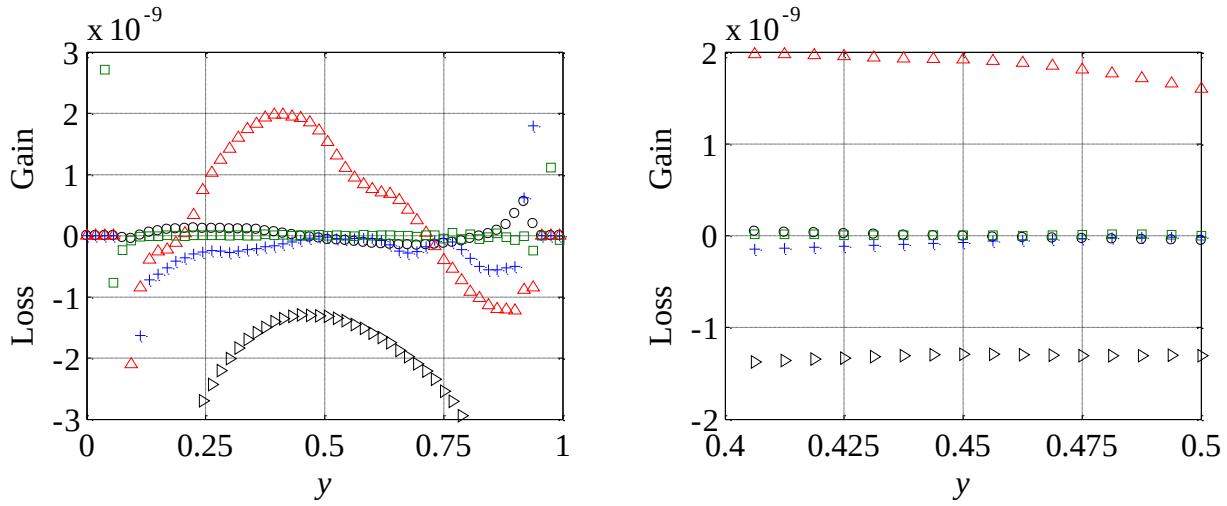

FIG. 16. Budget of Reynolds shear stress $\langle v^2 \rangle$ (a) across the annulus and (b) the magnified view at the centerline. Symbols: o, A_{22}; +, P_{22}; Δ, T_{22}; □, D_{22}; ▷ , ε_{22}.

V. SPATIAL SCALE OF COHERENT STRUCTURES

The streamwise length scale of turbulent fluctuations is investigated using spatial cross-correlation of u and v following

$$R_{uu} = \frac{\langle u_{(r_0,x)} u_{(r_0,x+\Delta x)} \rangle}{\langle u^2 \rangle} \tag{25}$$

where $u_{(r0,\,x)}$ is a one-dimensional matrix of u at radial location of r_0 extending over the streamwise extent of the measurement domain, i.e. over 14.180 mm (Δy = 0.475). Δx is the streamwise displacement which is selected 0.746 mm (Δy = 0.025). An equation similar to R_{uu} is also used to obtain R_{vv}. The correlation coefficients R_{uu} and R_{vv} are plotted for r_0 values along the radial axis in Figures 17 and 18, respectively.

The streamwise fluctuations are observed to have a smaller streamwise extent in the vicinity of the inner and outer walls of Figure 17(a). The length scale becomes larger as the distance from the wall increases and R_{uu} reaches local maximum at about y = 0.2 and 0.85 on the inner and outer sides of the annuli, respectively. The correlation length scale decreases as y increases further toward the midsection. R_{uu} reaches local minimum at y = 0.4562 where it overlaps with y_U. This reduction of streamwise

correlation toward the middle of the annulus is attributed to the blend of the structures from the two wall flows. Therefore, the location of $<U>_{max}$ is where maximum mixing of the structures from the two walls occurs. The streamwise extent of radial fluctuations (v) investigated in Figure 18 using R_{vv} is observed to be small in the vicinity of the walls and reach the maximum length-scale at about $y = 0.55$.

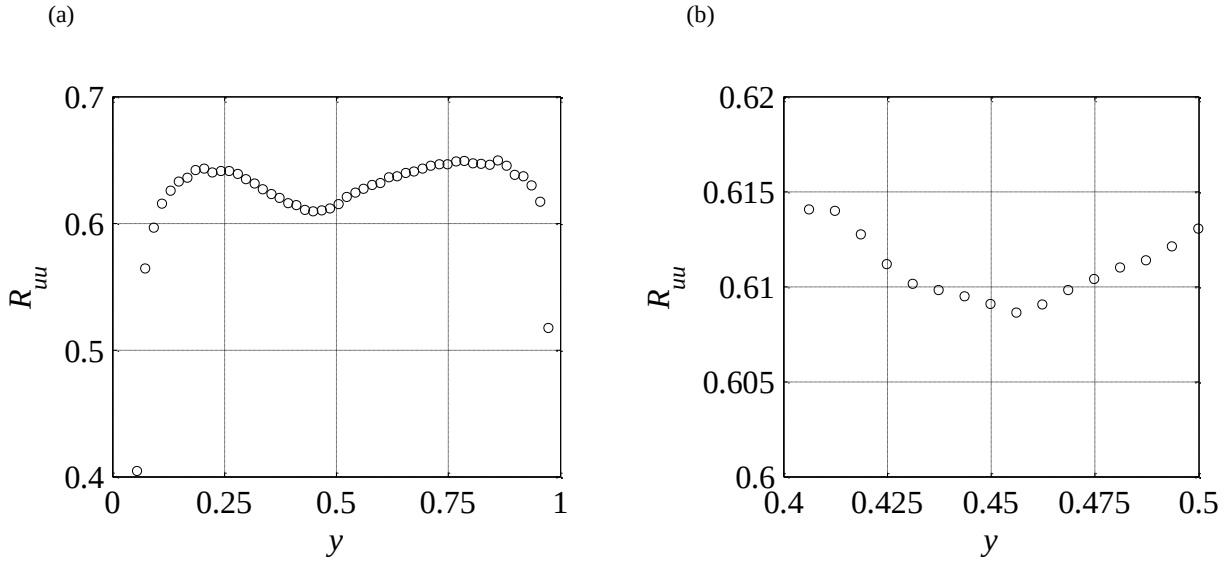

FIG. 17. Streamwise spatial-correlation of u (a) across the annuli and (b) at the midsection.

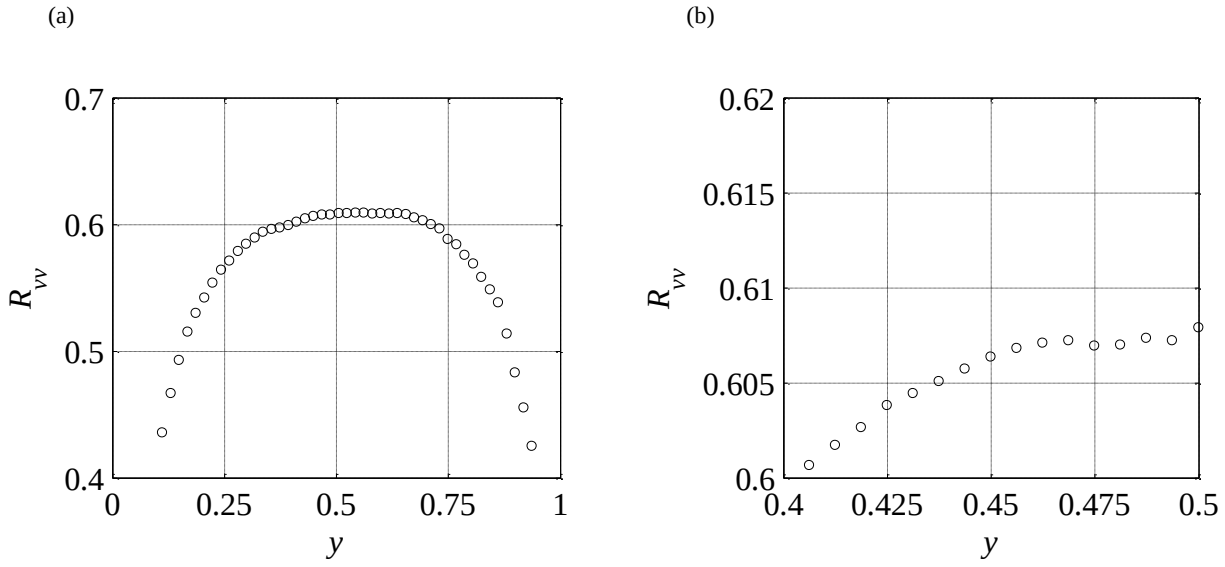

FIG. 18. Streamwise spatial-correlation of v (a) across the annuli and (b) the central region.

VI. DISCUSSION

The formation of a zone of negative production of turbulence kinetic energy has been discussed by Hussain (1986) using the coherent structures approach. Hussain [33] associated the negative production with counter-gradient momentum transport by coherent vortical structures which are stretched along the principal strain axis of the average velocity field (see figure 10 of Hussain [33]). These vortical structures produce a dominant fluctuation in $Q1$ and $Q3$ quadrants (positive <uv>) and consequently negative production in a velocity field with positive $\partial\langle U\rangle/\partial y$. Although there are $Q1$ and $Q3$ events in wall flows, typically the turbulent producing events of $Q2$ and $Q4$ dominate and result in net production of turbulent kinetic energy. In a channel flow, at any instant in which a $Q2$ or a $Q4$ event crosses y_U (location of $\langle U\rangle_{max}$) to the other side where $\partial\langle U\rangle/\partial y$ has an opposite sign, there would be a negative production of turbulence. This process is shown in Figure 19 by observing the turbulence production of the large negative *uv* event of the inner wall (stretched from $y = 0.25$ up to about 0.6 in Figure 19(a)). The lower part of this structure ($y < y_U$) contributes to positive turbulence production while the upper part contributes to negative turbulence production ($y > y_U$) on the average mean flow profile as observed in Figure 19(b). The same holds for ejection and sweep events of the upper wall ($Q3$ and $Q1$, see Figure 8). These events contribute to negative production of turbulence if they are located at $y < y_U$. In a symmetric channel flow, the negative turbulence production events of the top and bottom walls (or inner and outer walls) cancel out. However, in an asymmetric channel flow (such as an annuli flow) a region of slight negative production remains on the side of y_U with thinner boundary layer and extends to y_{uv} as observed in Figure 15(b).

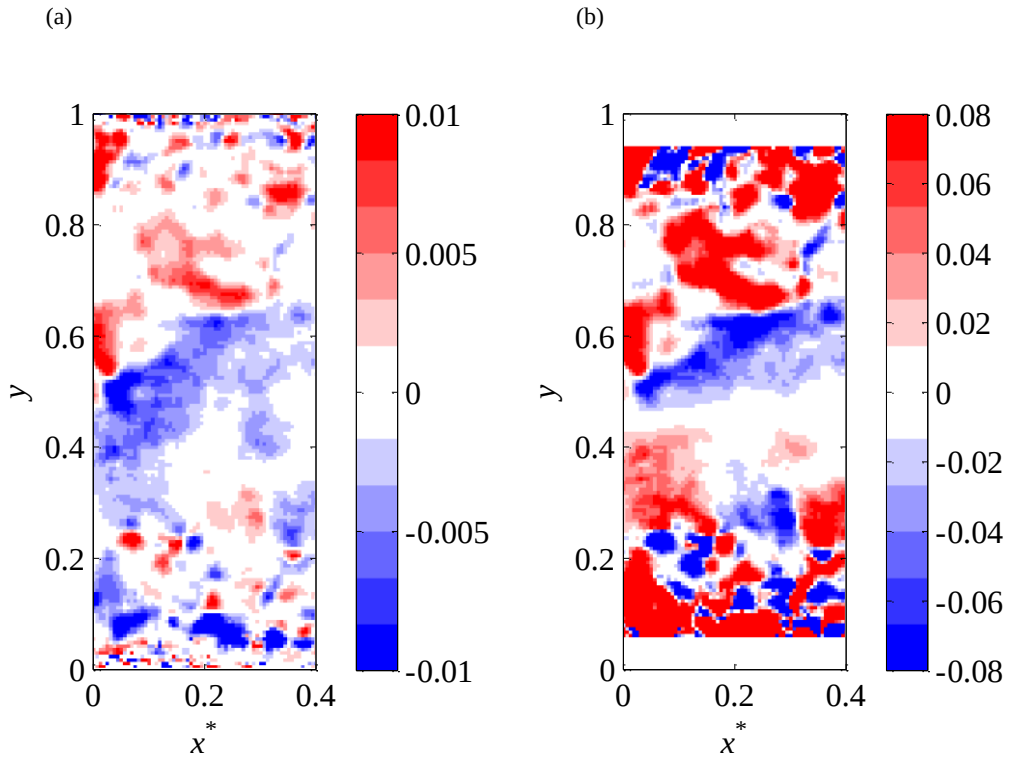

FIG. 19. Instantaneous contour plot of (a) uv [m^2/s^2] and (b) $uv\ \partial\langle U\rangle/\partial y$ [m^2/s^3] across the annulus. The ejection/sweep events (negative uv) of the lower wall contribute to negative turbulence production if they are located at $y > y_U$ (=0.456). For example, the negative uv patch observed at about y = 0.5 till 0.6 is associated with negative turbulence production. The top and bottom part of (b) is removed due to high noise level of the data in the close vicinity of the wall (white margin).

The region with negative production of turbulence is expected to have a significant role in smoothing the profiles of the two boundary layers at their joining point which is at $\langle U\rangle_{max}$ (see Figure 4(a)). This is investigated through the streamwise component of the Reynolds-averaged Navier-Stokes (RANS) equation for a stationary flow ($\partial/\partial t = 0$) after neglecting the third components ($\partial/\partial z$ and W) for simplicity

$$\rho\langle U\rangle\frac{\partial\langle U\rangle}{\partial x}+\rho\langle V\rangle\frac{\partial\langle U\rangle}{\partial y}=-\frac{\partial P}{\partial x}+\mu\frac{\partial^2\langle U\rangle}{\partial x^2}+\mu\frac{\partial^2\langle U\rangle}{\partial y^2}+\rho\frac{\partial\langle u^2\rangle}{\partial x}+\rho\frac{\partial\langle uv\rangle}{\partial y} \quad (26)$$

In a fully developed pipe/channel, both the first ($\langle U\rangle$ and $\langle V\rangle$) and the second order statistics ($\langle u^2\rangle$, $\langle v^2\rangle$, $\langle uv\rangle$) should not change in the streamwise direction ($\partial/\partial x = 0$). In combination with the continuity equation, the left side of equation 26 and the second and forth terms of its right side would be zero. The pressure gradient term and the $\partial\langle uv\rangle/\partial$y term also become constant in the midsection of a fully developed

pipe or channel flow. The former would be equal to the streamwise gradient at the wall $\partial P/\partial x = \partial P_w/\partial x$ and the latter is due to the linear distribution of $<uv>$. Therefore, the curvature ($\partial^2<U>/\partial y^2$) would be constant in the midsection of a fully developed pipe or channel flow. However, in the annular flow of the current experiment, the curvature ($\partial^2<U>/\partial y^2$) changes in the vicinity of $<U>_{max}$ with larger negative value on the left side of y_U as shown Figure 20(a). It is also observed in Figure 20(b) that the dominant terms, which are the left side terms, and the $\partial<uv>/\partial$y term are not zero. Therefore, although the current investigation is carried out at a relatively long entrance length of L/d_h=97, the illustrated terms of Figure 20(b) have a finite value indicating deviation from the fully developed condition. It is conjectures that upon achieving the fully developed state, $\partial^2<U>/\partial y^2$ would be equalized on both sides of $<U>_{max.}$

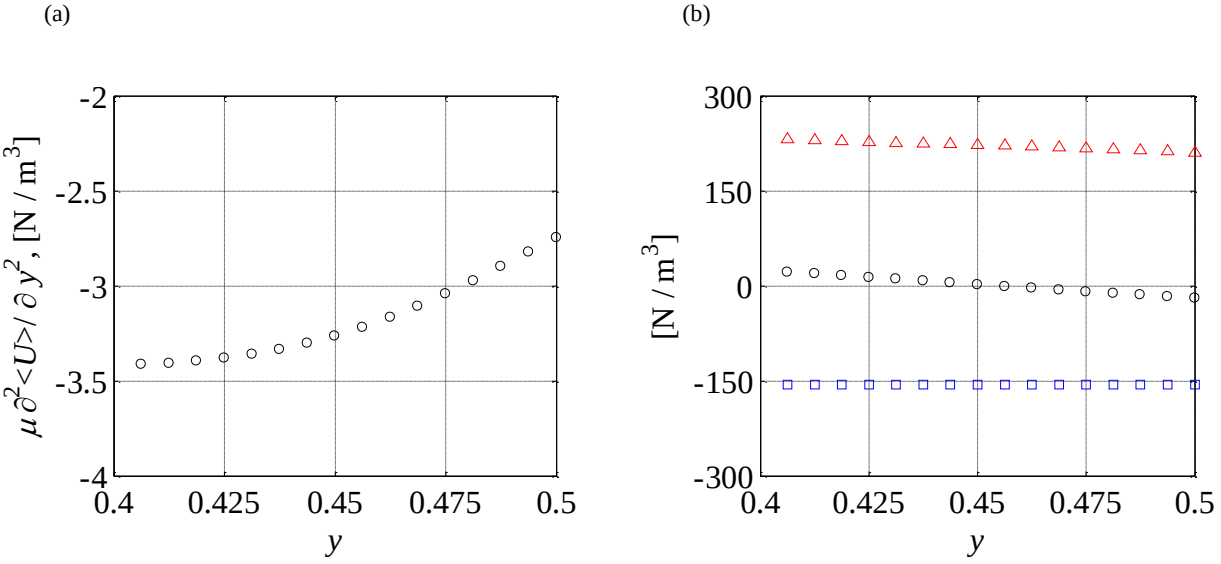

FIG. 20. Profiles of (a) curvature of the mean velocity profile and (b) $\rho<V>\partial<U>/\partial y$ (with o symbol), $\rho<U>\partial<U>/\partial x$ (with □ symbol), and $\rho\,\partial<uv>/\partial y$ (with Δ symbol) of the streamwise RANS (equation 26) in mid-section of the annuli. $\partial<U>/\partial x$ is estimated from measurement of $\partial<V>/\partial y$ in combination with the continuity equation.

The lack of fully developed flow may have caused the observed non-coincidence in the previous literature. The experiments of Lawn & Elliot [6] was carried out at L/d_h of 45 to 68, Rehme [7] at L/d_h of 77 to 83, and Nouri *et al.* [1] at L/d_h of 116 all showing non-coincidence of y_U, y_{uv}, y_{u2}, y_{v2} at the midsection of the annuli. The asymmetric channel flow experiments of Hanjalic & Launder [10] is estimated to have carried out at maximum L/H of 110 and the experiment of Burattini *et al.* [12] at L/H of

75 where H is the full channel height. Therefore, the non-coincidence of the y_U, y_{uv}, y_{u2}, y_{v2} at the midsection of the annuli might be associated with lack of complete spatial development of the flow field. The region of negative production of turbulence forms between y_U and y_{uv} and smooths the curvature of $\langle U \rangle$ at the joining point of the two boundary layers. This is hypothesized to gradually overlaps y_U, y_{uv}, y_{u2}, y_{v2} locations with streamwise development of the flow.

VII. CONCLUSION

The coincidence of the location of maximum velocity (y_U) and zero Reynolds shear stress (y_{uv}) is investigated in the asymmetric turbulent annular flow of a large-scale facility at Re = 59,200 to 90,800 using PIV and PTV measurements. The measurements are also applied to investigate the turbulent structure at the midsection of the annuli where the two boundary layers of the inner and outer walls merge. The results show that the location of y_U and y_{uv} do not overlap. In addition, the local minimum of $\langle u^2 \rangle$ and $\langle v^2 \rangle$ are also observed to approximately coincide with $\langle uv \rangle = 0$ while they are apart from $\langle U \rangle_{max}$ location. Error analysis shows that the difference of the locations is larger than the uncertainty of the measurement system.

The conditional averages of turbulent fluctuations of the four quadrants across the annuli demonstrated that the inner and outer wall boundary layers overlap each other in the midsection at least over a region of $\Delta y \approx 0.19$ wide. This overlap region at the mid-section of the annuli is subject to sweep/ejection events of both inner and outer walls while the investigation of the triple products shows that the ejections are the dominant mechanism of turbulence transport. The location of y_{uv} is observed where the opposite quadrant events of the two boundary layers cancel out and does not specify the outer edge of the inner or the outer wall flows. The local minimum of spatial correlation of u in the midsection of the annuli overlaps with y_U which demonstrates maximum mixing of the two boundary layers at this location.

Investigation of the budget of Reynolds shear stress showed that production and advection term acts towards the coincidence of the y_U and y_{uv} while the dissipation terms works against the coincidence of the two pointes. The location of $<U>_{max}$ was also observed to overlap with zero dissipation of $<uv>$. The production of turbulent kinetic energy is slightly negative in the narrow region between y_U and y_{uv}. The negative production of turbulence acts towards smoothing the mean velocity profile by equalizing the curvature ($\partial^2<U>/\partial y^2$) on the two sides of y_U across the $<U>$ profile. It is hypothesized that this non-coincidence is due to slight deviation from the fully developed condition

ACKNOWLEDGEMENTS

This work has been supported by the Natural Sciences and Engineering Research Council of Canada (NSERC RGPAS 411966 KURU and NSERC RGPIN 238623 KURU, and NSERC RGPIN 1512 GHAEMI).

APPENDIX A: STATISTICAL CONVERGENCE OF PIV DATA

In order to further assure the accuracy of PIV measurement in determining the location of $<U_{max}>$, $<uv> = 0$, $<u^2>_{min}$, and $<v^2>_{min}$, the cumulative averages of points A ($y = 0.4187$), B ($y = 0.4375$), C ($y = 0.4562$), and D ($y = 0.4688$) as indicated in Figure 5 are plotted versus the number of samples in Figure 20. The plots demonstrate both low and high frequency variation of averages with the number of samples. The low frequency variations relative to the absolute values within the sample range of Figure 21 are about 0.3% for $<U>$, 7% for $<uv>$ and less than 2% for $<u^2>$ and $<v^2>$. The error is mainly associated with both statistical convergence and unsteadiness of the pump during the PIV acquisition (approximately 20 minutes). The fluctuations of the average flow cause slight deviation from stationary flow assumption. The high frequency fluctuations of the average values are smaller than the low frequency fluctuations and are due to random error of the PIV measurement. Although the averages vary with the number of samples, it is observed that the relative magnitude of the values stay in the same order

for the considered neighboring locations of A, B, C and D. For example in Figure 21(a), point C remains as the maximum velocity while point B as $\langle uv \rangle = 0$ for the investigated number of samples.

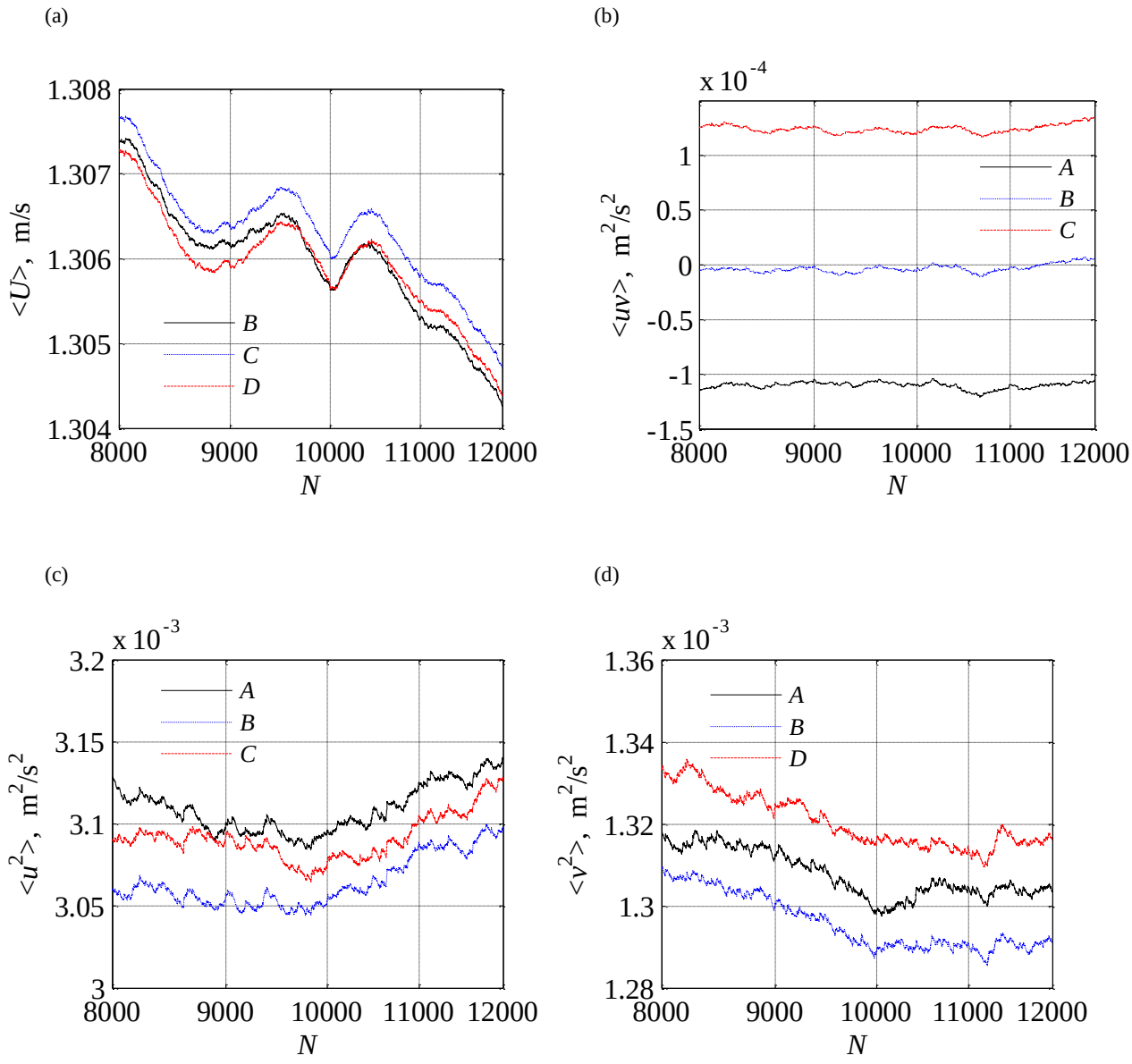

FIG. 21. The convergence of (a) $\langle U \rangle$, (b) $\langle uv \rangle$, (c) $\langle u^2 \rangle$, and (d) $\langle v^2 \rangle$ versus number of samples for radial positions A, B, C, D located at y = 0.4187, 0.4375, 0.4562, and 0.4688, respectively.

REFERENCES

[1] Nouri, J. M., Umur, H., & Whitelaw, J. H. Flow of Newtonian and non-Newtonian fluids in concentric and eccentric annuli. Journal of Fluid Mechanics, 253, 617-641 (1993).

[2] Crookston, R. B., Rothfus, R. R., & Kermode, R. I., Turbulent heat transfer in annuli with small cores. International Journal of Heat and Mass Transfer, 11(3), 415-426 (1968).

[3] Brighton, J. A., & Jones, J. B. Fully developed turbulent flow in annuli. Journal of Basic Engineering, 86(4), 835-842 (1964).

[4] Boersma, B. J., & Breugem, W. P. Numerical Simulation of Turbulent Flow in Concentric Annuli. Flow, Turbulence and Combustion, 86(1), 113-127 (2011).

[5] Maubach, K., & Rehme, K. Negative eddy diffusivities for asymmetric turbulent velocity profiles. International Journal of Heat and Mass Transfer, 15(3), 425-432 (1972).

[6] Lawn, C. J. & Elliott, C. J. Fully developed turbulent flow through concentric annuli. Journal of Mechanical Engineering Science, 14(3), 195-204 (1972).

[7] Rehme, K.. Turbulent flow in smooth concentric annuli with small radius ratios. Journal of Fluid Mechanics, 64(02), 263-288 (1974).

[8] Rodriguez-Corredor, F. E. R., Bizhani, M., Ashrafuzzaman, M., & Kuru, E., An experimental investigation of turbulent flow in concentric annulus using particle image velocimetry technique. Journal of Fluid Engineering, 136(051203), 1-11 (2014).

[9] Chung, S. Y., Rhee, G. H., & Sung, H. J. Direct numerical simulation of turbulent concentric annular pipe flow: Part 1: Flow field. International Journal of Heat and Fluid Flow, 23(4), 426-440, (2002).

[10] Hanjalic, K., & Launder, B.E., Fully developed asymmetric flow in a plane channel. Journal of Fluid Mechanics, 51, pp 301-335 (1972).

[11] Nagano, Y., Hattori, H., & Houra, T. DNS of velocity and thermal fields in turbulent channel flow with transverse-rib roughness. International journal of heat and fluid flow, 25(3), 393-403 (2004).

[12] Burattini, P., Leonardi, S., Orlandi, P., and Antonia, R.A. (2008), "Comparison between experiments and direct numerical simulations in a channel flow with roughness on one wall", Journal of Fluid Mechanics, 600, pp. 403–426.

[14] Laufer, J. The structure of turbulence in fully developed pipe flow. National advisory committee for aeronautics, Technical Note 2954 (1953).

[15] Kruka, V. & Eskinazi, S., The wall-jet in a moving stream. Journal of Fluid Mechanics, 20(04), 555-579 (1964).

[16] Wilson, D. J. Turbulent transport of mean kinetic energy in countergradient shear stress regions. Physics of Fluids (1958-1988), 17(4), 674-675 (1974).

[17] Palmer, M. D., & Keffer, J. F. An experimental investigation of an asymmetrical turbulent wake. Journal of Fluid Mechanics, 53(04), 593-610 (1972).

[13] Kundu, P., Cohen, I. & Dowling, D. Fluid Mechanics. 5th ed., Elsevier Science, page 557 (2012).

[18] Törnblom, O. Experimental and computational studies of turbulent separating internal flows." Doctoral thesis, Royal Institute of Technology, Stockholm, Sweden, (2006).

[19] Eskinazi, S. & Erian, F. F., Energy Reversal in Turbulent Flows, Physics of Fluids, 12, 1988-1998 (1969).

[20] Tennekes, H., & Lumley, J. L. (1972). A first course in turbulence. MIT press.

[21] Rehme, K.. Turbulence measurements in smooth concentric annuli with small radius ratios. Journal of Fluid Mechanics, 72(01), 189-206 (1975).

[22] Lu, S. S. & Willmarth, W. W. Measurements of the structure of the Reynolds stress in a turbulent boundary layer. Journal of Fluid Mechanics, 60(03), 481-511 (1973).

[23] Scarano, F. & Riethmuller M.L. Advances in iterative multigrid PIV image processing. Experiments in Fluids 29.1 (2000): S051-S060.

[24] Maas, H. G., Gruen, A., & Papantoniou D. Particle tracking velocimetry in three-dimensional flows Part I: Photogrammetric determination of particle coordinates, Experiments in Fluids 15 (1993): 133-146.

[25] Malik, N. A., Dracos, Th., Papantoniou D. Particle tracking velocimetry in three-dimensional flows Part II: Particle tracking, Experiments in Fluids 15 (1993): 279-294.

[26] Meinhart, C. D., Wereley, S. T., & Santiago, J. G. A PIV algorithm for estimating time-averaged velocity fields. Journal of Fluids Engineering, 122(2), 285-289 (2000).

[27] Clauser, F. H., The turbulent boundary layer. Advances in Applied Mechanics, 4, 1-51, (1956).

[28] Kaneda, M., Yu, B., Ozoe, H. & Churchill, S. W.. The characteristics of turbulent flow and convection in concentric circular annuli. Part I: flow. International journal of heat and mass transfer, 46(26), 5045-5057 (2003).

[29] Lavoie, P., Avallone, G., De Gregorio, F., Romano, G. P., & Antonia, R. A. Spatial resolution of PIV for the measurement of turbulence. Experiments in Fluids, 43(1), 39-51, (2007).

[30] Stanislas, M., Perret, L., & Foucaut, J. (2008). Vortical structures in the turbulent boundary layer: a possible route to a universal representation. Journal of Fluid Mechanics, 602, 327-382.

[31] Jung, S. Y., & Sung, H. J., Characterization of the three-dimensional turbulent boundary layer in a concentric annulus with a rotating inner cylinder. Physics of Fluids (1994-present), 18(11), 115102 (2006).

[32] Mansour, N. N., Kim, J. & Moin, P. Reynolds-stress and dissipation-rate budgets in a turbulent channel flow. Journal of Fluid Mechanics, 194, 15-44 (1988).

[32] Hussain, A. K. M. Coherent structures and turbulence. Journal of Fluid Mechanics, 173, 303-356 (1986).

[33] Quarmby, A. An experimental study of turbulent flow through concentric annuli. International Journal of Mechanical Sciences, 9(4), 205-221 (1967).